

ARTICLE

Open Access

Efficient TADF-based blue OLEDs with 100% stretchability using titanium particle-embedded indium zinc oxide mesh electrodes

Tae Hoon Park¹, Wanqi Ren¹, Ho Jin Lee¹, Nahyun Kim¹, Kyung Rock Son¹, Adila Rani¹ and Tae Geun Kim¹

Abstract

A highly stretchable and transparent electrode is a key element for realizing stretchable organic light-emitting diodes (SOLEDs). To date, several reports have been made on this issue; however, a sufficiently high mechanical stability (i.e., 100% stretchability) has not yet been demonstrated. Herein, we propose a titanium particle-embedded indium zinc oxide (Ti/IZO) mesh electrode fabricated on a Norland optical adhesive (NOA) substrate for the realization of mechanically robust and efficient SOLEDs. Initially, the geometry of the Ti/IZO mesh electrode is optimized based on the simulation and experimental results, which provides a high transmittance (92.5% at 480 nm), low sheet resistance (22.1 Ω /sq), and excellent mechanical stability (no substantial loss under 100% strain; only a 20% resistance change after 1000 stretching cycles), along with a work function of approximately 5.0 eV. Next, Ti/IZO mesh-based thermally activated delayed-fluorescence blue SOLEDs fabricated on NOA substrate are transferred onto prestretched 3 M VHB tape for mechanical testing. Interestingly, the devices stably operate under 100% tensile strain and exhibit an external quantum efficiency of 13.2%, which is 30 and 29% higher than those of devices with IZO and indium tin oxide planar electrodes, respectively. The reduced waveguide mode at the interface and increased outcoupling via corrugated metal islands are attributed to the observed improvement in performance.

Introduction

Stretchable optoelectronics are widely used in smartwatches, wearable devices, stretchable and textile displays, and health care systems^{1–5}. However, unlike curved displays or flexible smartphones that have only slight curvatures, stretchable devices need to maintain their efficiency under various mechanical deformations, such as folding, twisting, shrinking, and stretching^{6–8}. To fabricate these stretchable devices, all components, including the substrate, organic materials, and electrodes, that constitute the device must be mechanically stretchable. The substrate should be chemically and mechanically stable. Substrate candidate groups include rubber¹, polyimide⁹, polyurethane¹⁰, polydimethylsiloxane¹¹, and Norland optical adhesive (NOA)^{6,12}. Furthermore, the substrate for bottom-emitting organic light-emitting

diodes (OLEDs) must be transparent and should satisfy the aforementioned conditions; thus, a highly transparent and stretchable NOA substrate is considered as the ideal material for bottom-emitting OLEDs. Moreover, organic materials are generally stretchable and can be readily applied in stretchable devices. However, OLEDs exhibit different efficiencies depending on the type of organic material. Luminescence mechanisms are categorized into fluorescence and phosphorescence mechanisms. Conventional fluorescent OLEDs exhibit an internal quantum efficiency (IQE) of up to 25%, while the IQE of phosphorescent OLEDs reaches up to 100%. However, the high cost and scarcity of the metals used in phosphorescent OLEDs continue to be problematic. To resolve these issues and improve the efficiency of OLEDs, thermally activated delayed fluorescence (TADF)-based active materials have been used for blue OLEDs^{13–15}. Compared to conventional materials, TADF materials of current interest exhibit 100% IQE because all of the triplets can be

Correspondence: Tae Geun Kim (tgkim1@korea.ac.kr)

¹School of Electrical Engineering, Korea University, Seoul 02841, Republic of Korea

© The Author(s) 2022



Open Access This article is licensed under a Creative Commons Attribution 4.0 International License, which permits use, sharing, adaptation, distribution and reproduction in any medium or format, as long as you give appropriate credit to the original author(s) and the source, provide a link to the Creative Commons license, and indicate if changes were made. The images or other third party material in this article are included in the article's Creative Commons license, unless indicated otherwise in a credit line to the material. If material is not included in the article's Creative Commons license and your intended use is not permitted by statutory regulation or exceeds the permitted use, you will need to obtain permission directly from the copyright holder. To view a copy of this license, visit <http://creativecommons.org/licenses/by/4.0/>.

used as excitons without platinum group metals¹⁶. In addition to these issues, stretchable transparent electrodes for bottom-emitting OLEDs should be considered to enhance the efficiency of stretchable OLED (SOLED) devices. In general, indium tin oxide (ITO) electrodes are used for organic/inorganic LEDs owing to their high transmittance and low sheet resistance¹⁷. However, the work function (WF = 4.6–7 eV) of ITO electrodes is lower than that of indium zinc oxide (IZO) electrodes. In addition, ITO exhibits brittle characteristics¹⁸. Hence, the application of ITO is hindered in flexible OLEDs and SOLEDs. IZO electrodes exhibit a high WF (~5.1 eV) as well as good optical and electrical properties¹⁹. Moreover, the fabrication of mechanically stretchable and optically transparent electrodes is important for obtaining high-performance stretchable electronic devices because the device performance is critically affected by the mechanical, electrical, and optical properties of the electrodes. Therefore, several groups have suggested graphene²⁰, metal nanowires^{21,22}, PEDOT:PSS²³ and metal nanomesh^{24–26} electrodes to address these issues. However, it is difficult to prepare a high-quality multilayer electrode with graphene, and Ag nanowires have problems related to junction resistance and oxidation. Moreover, metal nanomesh electrodes are affected by the Moiré effect and low transmittance^{21,27}. There have been some other efforts to utilize metal oxide-based mesh structures^{28,29} to compensate for the drawbacks of conventional metal nanomesh; however, all of them simply reported their potentials as flexible electrodes without any experimental verifications at the device level.

In this study, TADF-based blue OLEDs were fabricated on highly stretchable NOA substrate using Ti particle-incorporated IZO (Ti/IZO) mesh electrodes. A uniform array of IZO mesh structures was fabricated by simple photolithography. The sheet resistance of the IZO mesh electrode was relatively high and increased further with the open area ratio. We theoretically and experimentally optimized the mesh ratio and incorporated Ti particles in the open region to reduce the sheet resistance of the mesh structure while maintaining its high transmittance. On the other hand, a large number of photons generated from photoactive layers of the bottom-emitting OLED were observed to be wave-guided by a difference in refractive index when coupled out through the substrate. However, in the presence of Ti particles, the extracted light was scattered at an angle greater than the critical angle, thus improving the light outcoupling efficiency of OLEDs. The IZO mesh structure also led to a significant improvement in the stretchable characteristics compared with the ITO and IZO planar electrode devices. Consequently, the SOLED using a Ti/IZO mesh electrode exhibited both high external quantum efficiency (EQE) and luminance intensity regardless of the viewing angle.

Experimental section

Fabrication of the NOA substrate

The NOA 63 (Norland Products, Inc.) material was dropped on a 1-inch glass substrate using a pipette, spun-coated at a speed of 4000 rpm at room temperature, and then cured by UV for 5 min. After depositing the organic material onto the substrate, the four sides were cut and peeled off using tweezers.

Fabrication of the electrodes

Planar electrodes: ITO material was deposited with a thickness of 100 nm at a 2 Å/s growth rate, an 80 W RF power and a 5 mTorr working pressure, while IZO material was deposited with a thickness of 200 nm at a 2 Å/s growth rate, an 80 W RF power, and a 2 mTorr working pressure using an RF magnetron sputtering system.

Mesh electrodes: A 2-nm-thick Ti island layer was deposited on NOA substrate using an e-beam evaporator at a growth rate of 0.2 Å/s. After a simple photolithography process (positive photoresist: GXR-601, AZ Electronic Materials), a 200-nm-thick IZO layer was deposited on a mesh-patterned Ti-island/NOA substrate using an RF magnetron sputtering system at a rate of 2 Å/s. Finally, the Ti/IZO mesh structure was formed by removing the photoresist with acetone through sonication. The IZO mesh electrode was fabricated in the same manner as the Ti/IZO mesh but without Ti deposition.

Fabrication of TADF-based blue SOLEDs

To fabricate a TADF-based blue SOLED, organic materials (N,N-dicarbazoyl-3,5-benzene (mCP) as a hole transport layer, bis[4-(9,9-dimethyl-9,10-dihydroacridine) phenyl] sulfone (DMAC-DPS) as a photoactive layer, and bis[2-(diphenylphosphino)-phenyl] ether oxide (DPEPO) as an electron transport layer), inorganic materials (MoO₃ as a hole injection layer (HIL), LiF as an electron injection layer), and Al metal as a cathode were evaporated on the Ti/IZO mesh structure using a thermal evaporator system (Daedong High Technologies Co., Ltd) at below 2×10^{-7} Torr. The LiF was deposited at a rate of 1 Å/s, and the Al electrode was deposited at a rate of 5 Å/s, while all other organic materials and MoO₃ were deposited at a rate of 0.5 Å/s. All materials were deposited and patterned through shadow masks.

Characterization

The transmittance of each electrode was measured as a function of wavelength using a UV-vis spectrophotometer (Lambda 35, Perkin Elmer). The sheet resistance was measured using a four-point probe measurement system, while the stretch characteristics of each electrode were measured using a stretching tester (COAD.121E, Ocean Science). Furthermore, the

characteristics of each OLED, including the current density, voltages, luminance, EL intensity, EQE, and light output intensity, were measured according to the viewing angle using an OLED measurement system (M6100 with a Keithley 2400, McScience Inc.). The surface images and morphologies were measured using scanning electron microscopy (SEM) (SU-70, Hitachi, Ltd.) and AFM (XE-100, Park systems Corp.). The WF mapping images were measured using a Kelvin probe system (KP01, KP technology).

FDTD simulation

Finite-difference time-domain modeling was performed using a finite-difference time-domain (FDTD) simulation (FDTD solutions, Lumerical Inc.). The refractive index of each material was obtained using an ellipsometer in the wavelength range of 380–1050 nm (F20, Filmetrics Inc.). The transmission monitor was set on the substrate. The electric and near-field distribution was then observed through the frequency-domain field and power monitor. The simulation time for the results was set to 1000 fs.

Results and discussion

Figure 1a shows a schematic of the SOLED structure with the Ti/IZO mesh electrode. A stretchable substrate was prepared by coating the NOA material on a 1-inch × 1-inch glass (Fig. S1). When UV treatments were performed after coating, the NOA substrate exhibited a transmittance of ~99% at a wavelength of 480 nm (Fig.

S2). On the substrate, a 2-nm-thick Ti island was formed through an e-beam evaporator. Thereafter, IZO mesh patterns were designed and transferred onto the photoresist for photolithography. The mesh hole diameter was 10 μm, and the spacing was designed to be 10 μm. Subsequently, 200-nm-thick IZO was deposited through a radio-frequency (RF) magnetron sputtering system, followed by a lift-off process for the formation of the Ti/IZO mesh electrode. Next, 1-nm-thick MoO₃, 40-nm-thick mCP, 30-nm-thick DMAC-DPS, 50-nm-thick DPEPO, 0.8-nm-thick LiF, and 100-nm-thick Al were deposited sequentially using a thermal evaporator to fabricate the SOLED. Finally, the stretchable device was formed by peeling off the NOA substrate from the glass substrate. The NOA substrate is not a material that can be stretched up to 100% by itself when it is thermally treated. Therefore, the fabricated sample was attached to 3 M VHB tape that was prestretched, and the released state was regarded as the initial state, as indicated in Figure 1b. In other words, the sample was stretched from the wrinkled state to the original position. Figure 1c shows photographs of the SOLED before and after strain. Next, the thickness information of the fabricated SOLED was examined by cross-sectional SEM with a focused ion beam system and is depicted in Fig. 1d. Fig. 1e shows the highest occupied molecular orbital-lowest unoccupied molecular orbital energy levels of the OLED structure with the Ti/IZO electrode. Herein, the WF of the anodic IZO-based films (~5.1 eV) was higher than that of typical ITO (~4.74 eV)

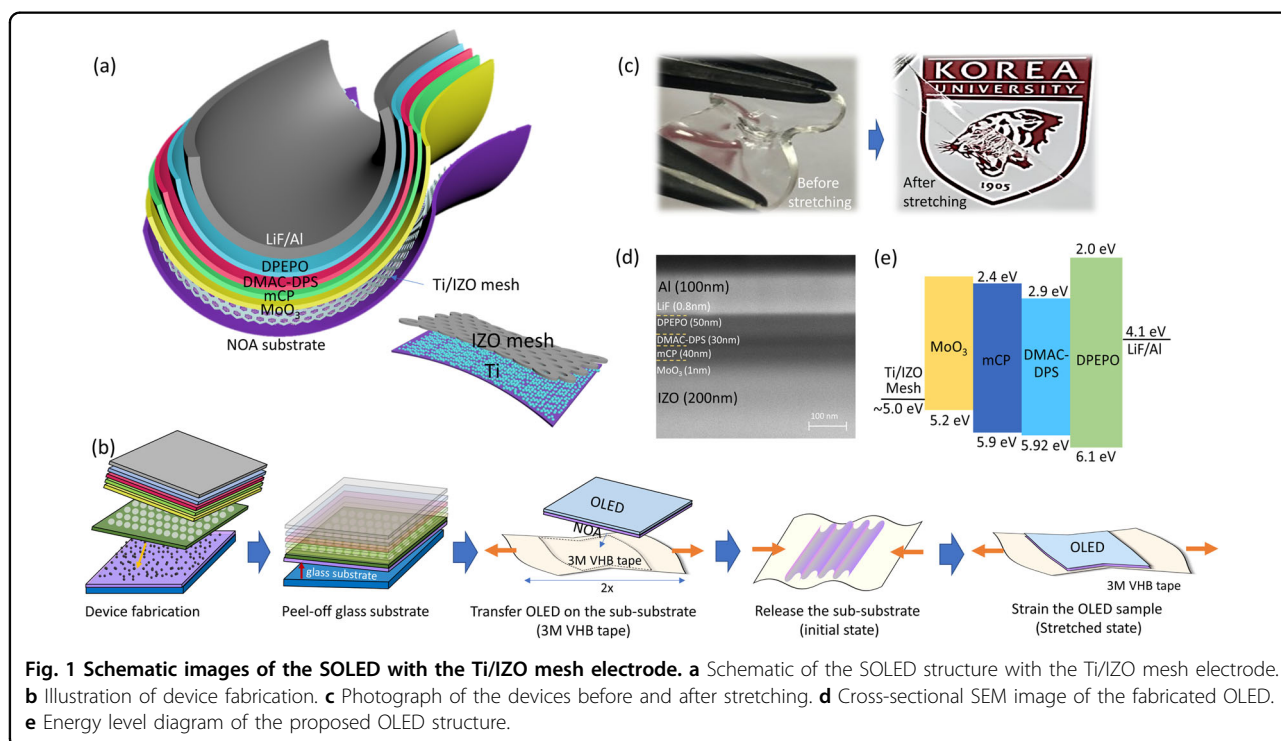


Fig. 1 Schematic images of the SOLED with the Ti/IZO mesh electrode. **a** Schematic of the SOLED structure with the Ti/IZO mesh electrode. **b** Illustration of device fabrication. **c** Photograph of the devices before and after stretching. **d** Cross-sectional SEM image of the fabricated OLED. **e** Energy level diagram of the proposed OLED structure.

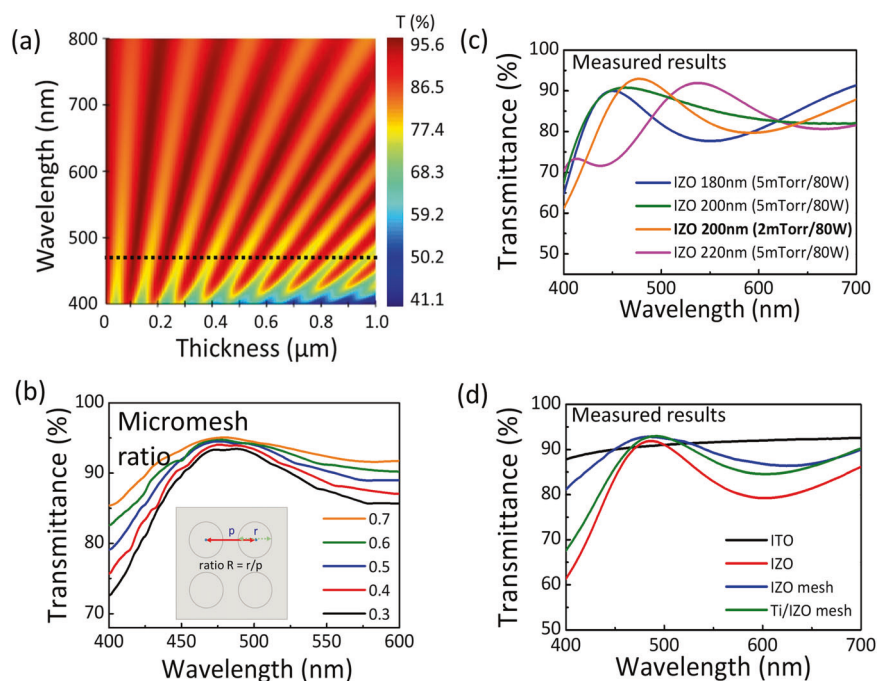


Fig. 2 Typical optical properties of the electrodes. **a** Contour plot for the transmittance of the IZO films as a function of the wavelength and film thickness using an FDTD simulation. **b** FDTD-simulated transmittance of the electrodes with different ratios of the micromesh structure. The inset represents the ratio of the mesh patterns. **c** Transmittance versus wavelength curves measured for IZO films with different thicknesses. **d** Measured transmittance of the ITO, IZO, IZO mesh, and Ti/IZO mesh electrodes.

and was expected to be beneficial for aligning the energy level of the film with that of the HIL (5.2 eV for MoO_3), facilitating hole injection efficiency.

Figure 2 shows the data related to the optimization of the mesh pattern electrode. Prior to fabrication, we investigated the optimal condition of the mesh structure in the IZO electrode (i.e., thickness, diameter and spacing of the pattern) through FDTD simulation. Fig. S3 shows a schematic for the FDTD simulation of the mesh-based OLED structure. Specifically, periodic boundary and perfectly matched layer conditions were applied to the x - and y -axes, respectively. The step of the mesh grid was $1 \text{ nm} \times 1 \text{ nm}$. The transmittance was calculated using a plane wave source, and the field intensity simulation was applied through the sum of the dipole sources in the x , y , and z directions after calculation.

First, we determined the optimal thickness of the IZO film using the calculated contour plot for the transmittance as a function of the wavelength and the thickness, as shown in Fig. 2a. The transmittance versus emission wavelength varied periodically with IZO thickness due to Fabry–Perot interference³⁰, where the highest transmittance was observed for 100- and 200-nm thick IZO films at a wavelength of 480 nm, as indicated by the dotted line (Fig. 2a). Next, the mesh electrode structure was simulated to determine the size and the periodicity of the mesh patterns based on the 200-nm thick IZO film. Figure 2b

shows the transmittance curves as a function of the diameter and spacing of the mesh structure, calculated via FDTD simulation. In this figure, the optical and electrical properties of the mesh electrode were found to vary with the diameter and spacing of the mesh structure. To theoretically investigate the correlation between the mesh diameter and the spacing, the mesh diameter was set as r , and the spacing between the two centers was set as p ; hence, their ratio = r/p . The simulation results regarding this ratio between the mesh diameter and the spacing indicates that the ideal transmittance can be observed at a ratio of 0.5. As the ratio increases, the open area increases, and accordingly, the transmittance increases; however, the sheet resistance significantly increases³¹. These results indicated the same trend for the nanoscale mesh structure as for the microscale mesh structure (Fig. S4). To further understand the effect of the pattern size on the optical properties of the mesh electrode, the transmittance was calculated for the nanomesh structure as well as the micromesh structure. As a result, for instance, the 250 nm mesh structure showed a 93.9% transmittance at 480 nm, while the 10- μm -wide mesh structure showed a 94.5% transmittance at 480 nm for the same ratio (Fig. S5)³². Therefore, we decided to use the micromesh electrode (with 10 μm diameter and 10 μm spacing between the patterns) because of its advantages in productivity as well as uniformity (or reproducibility) that are obtained

Table 1 Transmittance and sheet resistance values of the IZO films with different thicknesses and sputtering conditions.

IZO			Transmittance (%) @ 480 nm	Sheet resistance (Ω/sq)	
Thickness (nm)	Working pressure (mTorr)	RF power (W)			
100	5	80	88.2	29.1	
180	5	80	86.5	17.4	
200	2	40	87.2	18.3	
		80	91.6	16.2	
		120	88.1	16.9	
		5	40	87.1	18.9
			80	89.9	16.7
220	5	120	83.5	16.9	
		80	80.3	16.2	

without incurring losses in optical and electrical properties in regard to the fabrication of the mesh electrode.

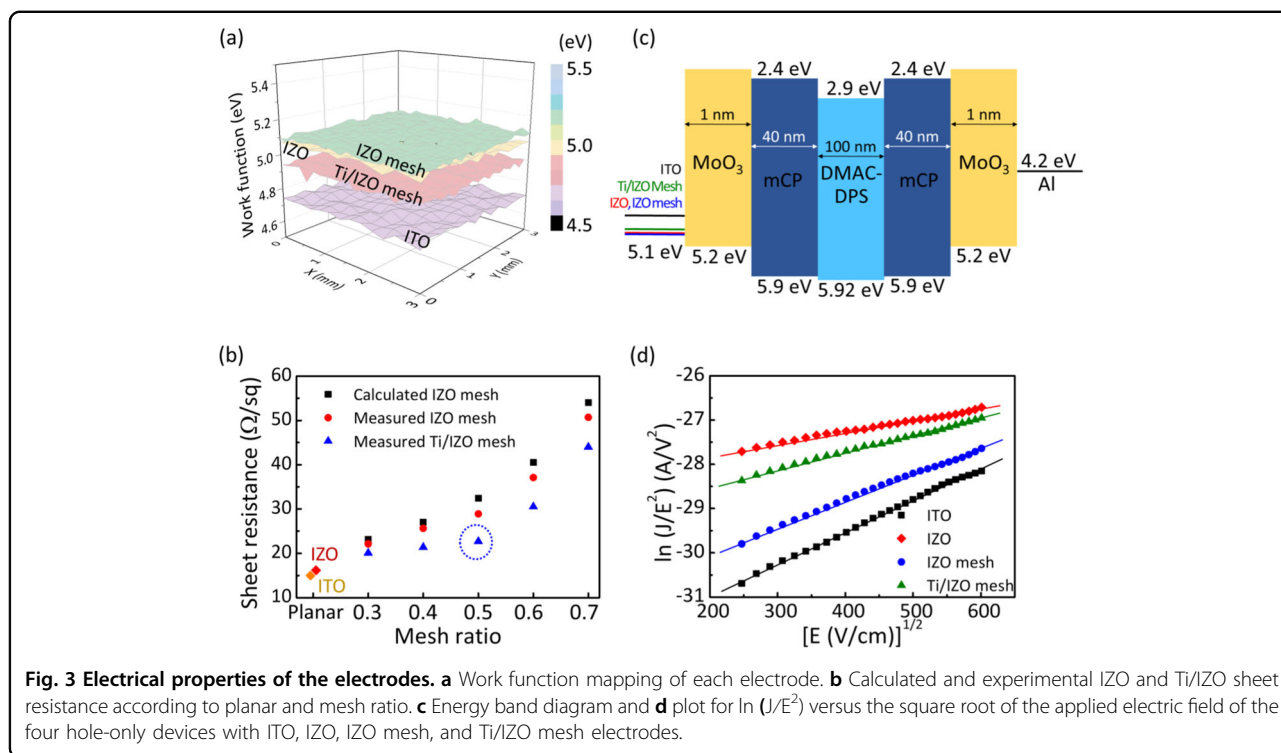
Based on the simulation results, we prepared 200-nm-thick IZO films deposited under different RF power (40, 80, and 120 W) and working pressure (2 and 5 mTorr) conditions and measured their transmittance (Fig. 2c) and sheet resistance, respectively, as summarized in Table 1. By comparison, a 200-nm-thick IZO film, deposited at an 80 W RF power and a 2 mTorr working pressure, was found to show the highest transmittance (91.6%) and the lowest sheet resistance (16.2 Ω/sq); therefore, the optimal IZO thickness was set at 200 nm. Regarding the deposition, all IZO films were initially deposited at a 5 mTorr working pressure and an 80 W RF power; then, the parameters, such as working pressure and RF power, were tuned up or down to find the optimal condition. Note that the crystallinity of metal-oxide films (i.e., IZO) generally decreases and the surface roughness increases as the working pressure increases; moreover, the carrier concentration decreases, and the Burstein-Moss effect, which narrows the energy band gap, was also observed. In addition, the electrical and optical properties were initially improved, but they were degraded at a certain point due to the increased scattering of ionized impurities. As the deposition power increases, the grain size increases with an energy higher than 120 W, the quality of the thin layer may deteriorate, and the adhesion to the substrate may decrease³³. Based on these optimal conditions of the sputtering system, the optical properties were examined by the deposition of the materials on the substrate by the sputtering system. Figure 2d shows the measured transmittance versus the wavelength of each electrode. The obtained results were similar to the simulation results (Fig. S6). The IZO planar and mesh structures exhibited a similar shape; however, the overall transmittance increased with the wavelength, and the additional Ti

structure revealed a transmittance loss at other wavelengths but no loss at the peak wavelength³⁴.

Figure 3a shows WF mapping images of the ITO, IZO, IZO mesh and Ti/IZO mesh electrodes captured over an area of $3 \times 3 \text{ mm}^2$ using a Kelvin probe system. The WF values obtained from this equipment were calibrated by using Ag as a reference sample ($\sim 4.6 \text{ eV}$). The WF of the ITO electrode was measured to be $4.74 \pm 0.03 \text{ eV}$, while the IZO and IZO mesh electrodes exhibited almost equivalent WF values of $5.09 \pm 0.03 \text{ eV}$ and $5.1 \pm 0.04 \text{ eV}$, respectively. The WF of the Ti/IZO mesh electrode was measured to be $4.97 \pm 0.08 \text{ eV}$, similar to that of IZO rather than that of Ti. This may be due to the use of a very thin Ti film. It is known that at least 6-nm-thick Ti films are required to illicit the WF behavior of Ti³⁵. Therefore, the WF of the Ti/IZO mesh electrode used in this study should be similar to that of the IZO electrode. Consequently, the WF matching (or band alignment) between the Ti/IZO mesh electrode and MoO_3 HIL leads to charge balance in the EML, enhancing the exciton coupling efficiency. Figure 3b shows the resistance change of each electrode with respect to the mesh ratio. Compared to the sheet resistance of ITO (15 Ω/sq) and IZO ($R_{\text{planar}} = 16.2 \text{ } \Omega/\text{sq}$) planar electrodes, IZO mesh patterned electrodes exhibited higher sheet resistance ($R' = 22.3\text{--}51.2 \text{ } \Omega/\text{sq}$) with an increase in the mesh ratio.

$$R' \approx \frac{1}{1 - \text{ratio}} R_{\text{planar}} \quad (1)$$

For example, the sheet resistance of the IZO mesh electrode increases by approximately 2 times compared to that of the IZO planar electrode at ratio = 0.5, according to Eq. (1)³³. The resistance changes of the fabricated IZO mesh electrode as a function of the mesh ratio were in good agreement with those of the calculated electrode. To



reduce the sheet resistance of the IZO mesh electrode, we deposited approximately 2-nm-thick Ti particles below the IZO surface. As a result, the sheet resistance of the Ti/IZO mesh electrode was reduced by the electrons hopping through the Ti particles laid between the IZO mesh holes³⁶, which might be beneficial for increasing the current injection. Interestingly, the sheet resistance of the IZO mesh electrode was reduced from 22.3 to 20.1 Ω/sq after incorporating Ti particles at a ratio of 0.3 and was steadily maintained up to a ratio of 0.5 in the range of 20.1–22.1 Ω/sq . However, it was increased significantly at a ratio of 0.6 or higher (i.e., 30.3 and 44.1 Ω/sq at a ratio of 0.6 and 0.7, respectively). Consequently, the sheet resistance of the IZO mesh decreased as the mesh ratio became small. However, considering the figure of merit (FoM) and mechanical properties, the Ti/IZO electrode with a mesh ratio of 0.5 was selected as the anode of the present TADF-based blue SOLED.

Next, we fabricated hole-only devices (HODs) with four different electrodes (ITO, IZO, IZO mesh and Ti/IZO mesh) to compare the hole-injection efficiency, as shown in Fig. 3c, d. Fig. 3c shows the energy band diagram of the HODs. The HOD structure consists of anodes (ITO, IZO, IZO mesh and Ti/IZO mesh)/ MoO_3 (1 nm)/mCP (40 nm)/DMAC-DPS (100 nm)/mCP (40 nm)/ MoO_3 (1 nm)/Al (100 nm)). In Fig. S7, the IZO planar electrode exhibits the highest current density among the four samples, which is followed by the Ti/IZO mesh, IZO mesh, and ITO electrodes. The sheet resistance of IZO is

slightly higher than that of ITO; however, the WF difference between IZO and HIL is much lower than that between ITO and HIL, increasing the hole-injection efficiency. The IZO mesh electrode has advantages in WF matching (or energy level alignment) with HIL as well as in transmittance when compared to ITO, but the increased sheet resistance due to the perforated structure offsets its advantages. Furthermore, the hole mobility of the device was analyzed by the space-charge-limited current (SCLC) method. The current density (J) in the SCLC regime can be expressed by the field-dependent modified Mott–Gurney equation as follows^{37,38}:

$$J = \frac{9}{8} \epsilon \epsilon_0 \mu_0 \frac{E^2}{L} \exp(0.89\beta\sqrt{E}) \quad (2)$$

where J denotes the current density, ϵ_0 is the permittivity of free space, ϵ corresponds to the relative dielectric constant, μ_0 is the zero-field mobility, E represents the electric field, L is the thickness of the active layer, and β denotes the field activation factor. The μ_0 and β of the HODs with four different electrodes can be extracted from the y-intercept and the slope of the fitted curves of $\ln(J/E^2)$ versus the square root of E (Fig. 3d), derived from Eq. 2 and the J - V curves in the SCLC regime of Fig. S7.

From Fig. 3d, the μ_0 values of the ITO-, IZO-, IZO mesh-, and Ti/IZO mesh-based devices are estimated to be $5.7 \times 10^{-9} \text{ cm}^2/\text{V}\cdot\text{s}$, $3.3 \times 10^{-7} \text{ cm}^2/\text{V}\cdot\text{s}$, $1.8 \times 10^{-8} \text{ cm}^2/\text{V}\cdot\text{s}$, and $1.3 \times 10^{-7} \text{ cm}^2/\text{V}\cdot\text{s}$, respectively. Specifically, the

μ_0 of the Ti/IZO mesh-based device is much higher than that of the ITO- and IZO mesh-based devices, although it is slightly lower than that of the IZO-based device owing to the perforated structure of the mesh electrode. On the other hand, the β value of the Ti/IZO mesh-based device is observed to be $4.5 \times 10^{-3} \text{ cm}^{1/2}/\text{V}^{1/2}$, which is smaller than that ($8.1 \times 10^{-3}, 6.9 \times 10^{-3} \text{ cm}^{1/2}/\text{V}^{1/2}$, respectively) of the ITO- and IZO mesh-based devices and slightly higher than that ($3.2 \times 10^{-3} \text{ cm}^{1/2}/\text{V}^{1/2}$) of the IZO-based device. However, the field mobility ($\mu(E) = \mu_0 \exp(\frac{\mu_0}{0.89\beta\sqrt{E}})$) of the Ti/IZO mesh-based device is calculated to be higher than that of ITO- and IZO mesh-based devices in the SCLC regime because of its significantly higher μ_0 value. This result indicates that the hole mobility of the Ti/IZO mesh-based device is higher than that of the ITO- and IZO mesh-based devices and even comparable to that of the IZO-based device. Therefore, the Ti/IZO mesh structure can overcome the issue related to the high resistance of the IZO mesh, which allows for the full utilization of the high transmittance, low sheet resistance, WF matching with the HIL (thus, high hole injection efficiency), and mechanical stretchability.

Table 2 shows the measured transmittance, sheet resistance and mechanical stability values of the present experimental set and those reported in the literature for comparison^{12,22,26,28–30,39–42}. The ITO, IZO planar, IZO mesh, and Ti/IZO mesh electrodes exhibited transmittance

values of 90.7%, 91.6%, 92.7%, and 92.5% at 480 nm and sheet resistances of 15, 16.2, 28.9, and 22.1 Ω/sq , respectively. In addition, the corresponding FoMs can be calculated from the transmittance (T) and sheet resistance (R_{sheet}) using the equation below⁴³.

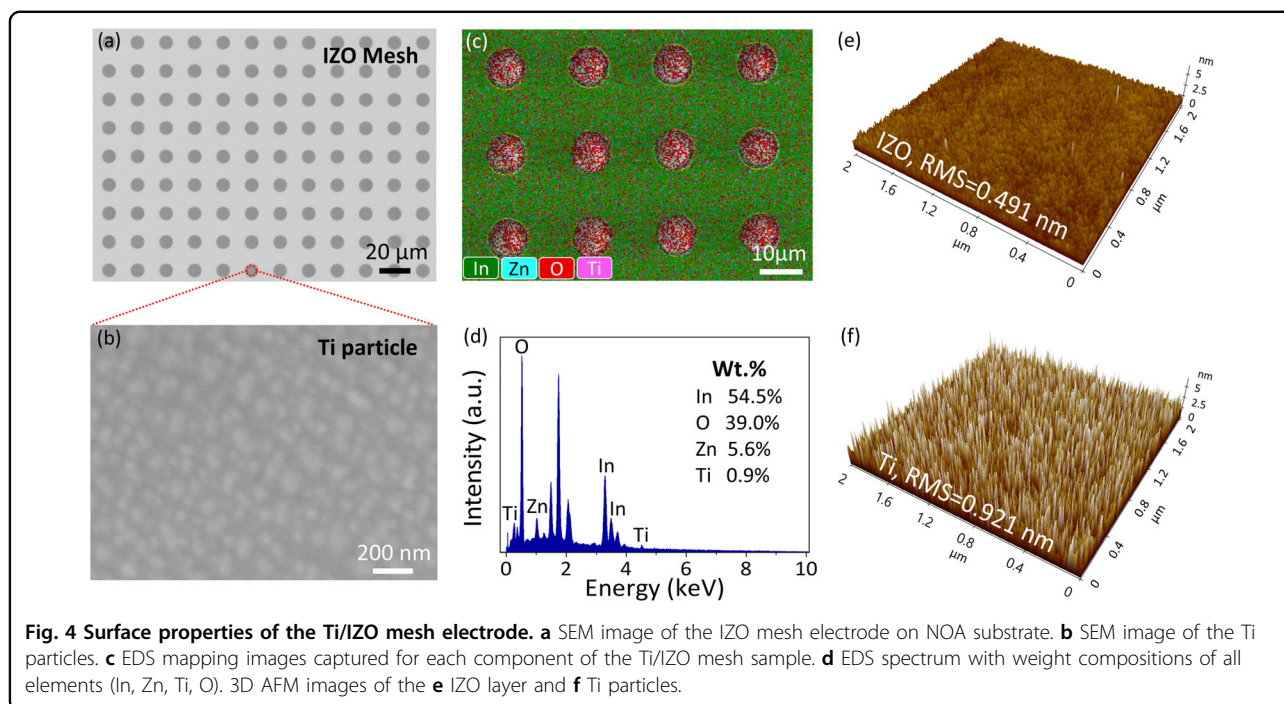
$$FoM = T^{10}/R_{\text{sheet}}(\Omega^{-1}) \tag{3}$$

The FoMs of each electrode were 0.0251, 0.0257, 0.0162, and 0.0208 Ω^{-1} . From previous studies, the FoMs are 0.00296 Ω^{-1} for MoO₃/Au/MoO₃¹², 0.0163 Ω^{-1} for AgNW/Graphene²², 0.007 Ω^{-1} for Au nanomesh²⁶, 0.0002 Ω^{-1} for ITO mesh²⁸, 0.0066 Ω^{-1} for ITO/Ag mesh/ITO²⁹, 0.0144 Ω^{-1} for Ag Fiber/IZO³⁰, 0.0029 Ω^{-1} for WO₃/Ag/WO₃⁴³, 0.0097 Ω^{-1} for TiO₂/Au/TiO₂, 0.0073 Ω^{-1} for TiO₂/Ag/TiO₂³⁹, 0.0038 Ω^{-1} for CuNW⁴⁰, 0.005 Ω^{-1} for MoCl₅-Graphene⁴¹ and 0.07 Ω^{-1} for AgNW⁴². By comparing the FoM values of all electrodes mentioned above, including those from previous reports, it was confirmed that the IZO-based electrodes have advantages in transmittance and sheet resistance compared to other electrodes. In particular, the Ti/IZO mesh electrodes are considered to be the most advantageous because the island-shaped Ti particles improve the electrical properties, while the mesh structure provides excellent mechanical properties. Based on these findings, we fabricated IZO-based mesh electrodes with island-shaped Ti particles using an RF sputtering system and

Table 2 Performance comparison of the proposed Ti/IZO mesh electrode with reference and previously reported stretchable and flexible electrodes.

Electrodes	Transmittance (% , Visible range)	Sheet resistance (Ω/sq)	FoM (Ω^{-1})	Mechanical stability
ITO (Ref.)	90.7	15	0.0251	-
IZO (Ref.)	91.6	16.2	0.0257	40% 1000 cycles
IZO mesh (Ref.)	92.7	28.9	0.0162	100% 1000 cycles
Ti/IZO mesh (This work)	92.5	22.1	0.0208	100% 1000 cycles
MoO ₃ /Au/MoO ₃ ¹²	75.06	19.21	0.00296	100% 100 cycles
AgNW/Graphene ²²	80	15	0.0163	70% 100 cycles
Au nanomesh ²⁶	82.5	21	0.007	50% 1000 cycles
ITO mesh ²⁸	70.5	151	0.0002	6.85 mm 1000 cycles*
ITO/Ag mesh/ITO ²⁹	85	30	0.0066	N/A
Ag fiber/IZO ³⁰	83.6	15.5	0.0144	5 mm 2000 cycles*
TiO ₂ /Au/TiO ₂ ³⁹	88.4	30	0.0097	2.5 mm 1000 cycles*
TiO ₂ /Ag/TiO ₂ ³⁹	93.5	72	0.0071	2.5 mm 1000 cycles*
Cu NW ⁴⁰	78	22.1	0.0038	10% 1000 cycles
MoCl ₅ -Graphene ⁴¹	88	54	0.005	30% 2000 cycles
Oriented AgNW ⁴²	85	2.8	0.07	40% 100 cycles

* Refs. 28,30,39 report the flexibility (not stretchability) of the metal/oxide electrode.



investigated the surface condition and uniformity of the fabricated mesh patterns via SEM analysis.

Figure 4a shows the SEM surface image of the Ti/IZO mesh patterns at a low magnification, by which the mesh patterns (with a 10 μm diameter and a 10 μm spacing) are uniformly fabricated on the IZO film. Figure 4b shows the SEM image of the Ti particles under the IZO mesh structure. By the deposition of a 2-nm-thick Ti layer at a low rate using the e-beam evaporator, an island shape was formed instead of a thin film. The size range of the resulting Ti islands was found to be from approximately a few nanometers to 200 nm. Figure 4c shows the energy-dispersive X-ray spectroscopy (EDS) mapping image of the mesh structure.

The EDS mapping images of each element are shown in Fig. S8. Owing to the IZO-material-based mesh structure, the presence of In and Zn was revealed by color mapping. In the case of oxide, oxygen was also detected on the NOA substrate, indicating that it is present in the entire area. As revealed in the aforementioned SEM image, Ti was observed as an island, but it was distributed over the entire area. The EDS spectrum of the Ti/IZO mesh electrode on the NOA63 substrate is shown in Figure 4d. EDS spectrum analysis was performed to determine the composition of the Ti particles dispersed on the surface. In particular, the measured K and L peak values of Ti were checked to confirm the quantitatively and qualitatively composed materials. As a result, each material of In, Zn, O and Ti on the surface was observed in atomic percentages of 54.5%, 5.6%, 39% and 0.9%, respectively. Figure 4e

and f show atomic force microscopy (AFM) images before and after Ti deposition, respectively. The root mean square (RMS) values of the IZO layer and the deposition of the Ti layer were 0.491 nm and 0.921 nm, respectively. Interestingly, the RMS value increased by approximately twice as much for the Ti particles, and an island was also formed (Fig. 3b). With the increase in the RMS value of Ti, the reflected beam of the emitted light toward the substrate can be extracted to a great extent because the produced Ti island caused a scattering effect that reduced the waveguide mode between the substrate and electrode. Moreover, the Ti/IZO mesh structure was the most suitable electrode because the mechanical stretchable properties are also important in stretchable devices.

To verify the electrical performance of each electrode as it was stretched, the change in the sheet resistance was measured under strains ranging from 0 to 100% and stretching ranging from 0 to 1000 cycles. Figure 5a presents the graph of the sheet resistance as a function of strain. In the case of the ITO electrode, owing to its brittle characteristics, the sheet resistance increased nearly 100 times even at a strain of only 10% and further increased nearly 10,000 times at a strain of 20%. For the IZO planar electrode, the sheet resistance increased 7 times at a strain of 30%. However, for the IZO mesh electrode, the sheet resistance increased by less than 2 times, even when the strain increased by 100%. Likewise, when the Ti/IZO mesh electrode was stretched by 100%, the sheet resistance also increased by less than 2 times; however, the sheet resistance did not change significantly because the

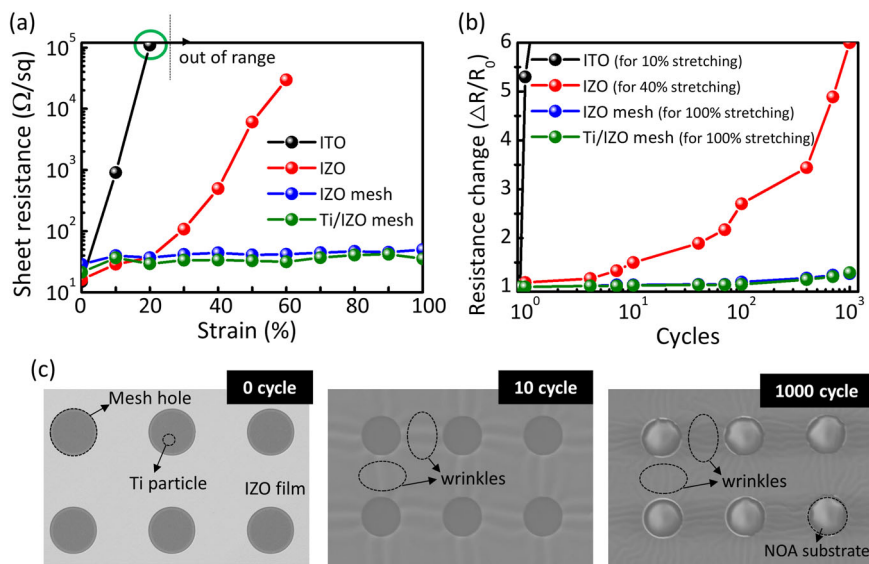


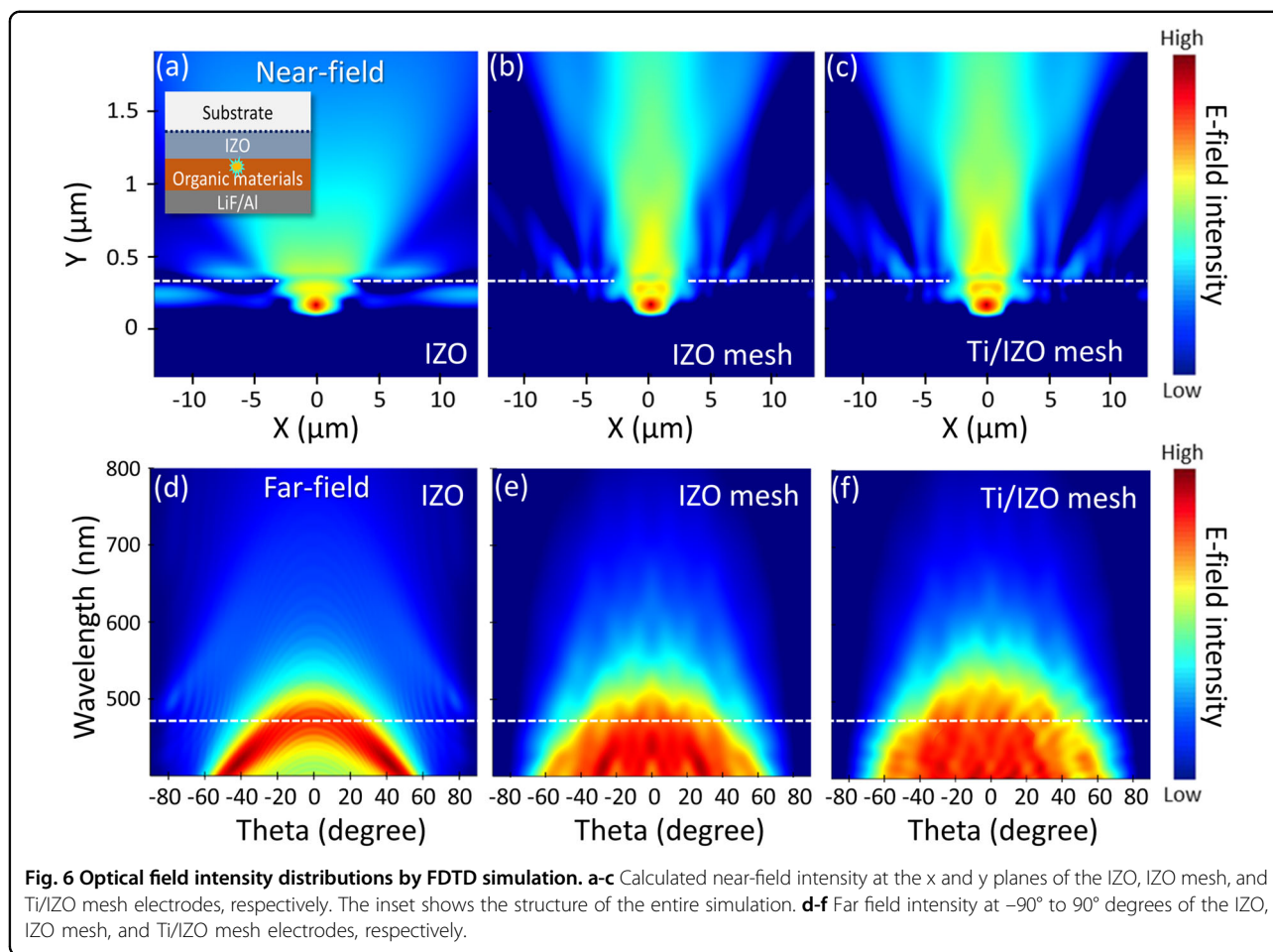
Fig. 5 Mechanical properties of the electrodes. **a** Sheet resistance changes versus the degree of strain for the ITO, IZO, IZO mesh, and Ti/IZO mesh electrodes on NOA substrate. **b** Relative resistance changes versus the number of stretching cycles from 0 to 1000 times measured for the ITO, IZO, IZO mesh, and Ti/IZO mesh electrodes. **c** SEM images captured for the Ti/IZO mesh electrode after 0 to 1000 stretching cycles.

Ti was already in the island form. Figure 5b shows the change in the resistance as a function of stretching cycles from 0 to 1000. The sheet resistance of the ITO electrode was too high to be measured even with a 10% increase, while that of the IZO planar electrode increased by more than 5 times when strained by 40% during 1000 cycles. However, after 100% straining of the IZO mesh and Ti/IZO mesh electrodes during 1000 cycles, the sheet resistance increased by only 1.29 times. Based on the previous results, Figure 5c shows the SEM images for the Ti/IZO mesh electrode after 0 to 1000 stretching cycles with 100% stretching. At deposition, the surface was clean, but after 10 cycles, some wrinkles were observed on the surface. Moreover, after 1000 cycles, the number of wrinkles increased. However, the mesh shape was still maintained, and the electrical/optical properties did not change significantly.

Figure 6 displays the near- and far-field intensity distributions of the OLEDs with three different anode electrodes (IZO, IZO mesh, and Ti/IZO mesh). Figure 6a-c shows the calculated near-field intensity of each device by FDTD simulation. In the case of the IZO-based OLED (Fig. 6a), the electric field distributions of the photons toward the outside of the substrate were found to be considerably weak due to the trapping of light by the waveguide mode. In contrast, the waveguide mode can be reduced for IZO mesh-based OLEDs, as shown in Fig. 6b, because the reflection angle of the photons changes due to the corrugated structure of the IZO mesh. Moreover, owing to the scattering effect via Ti particles, the trapped

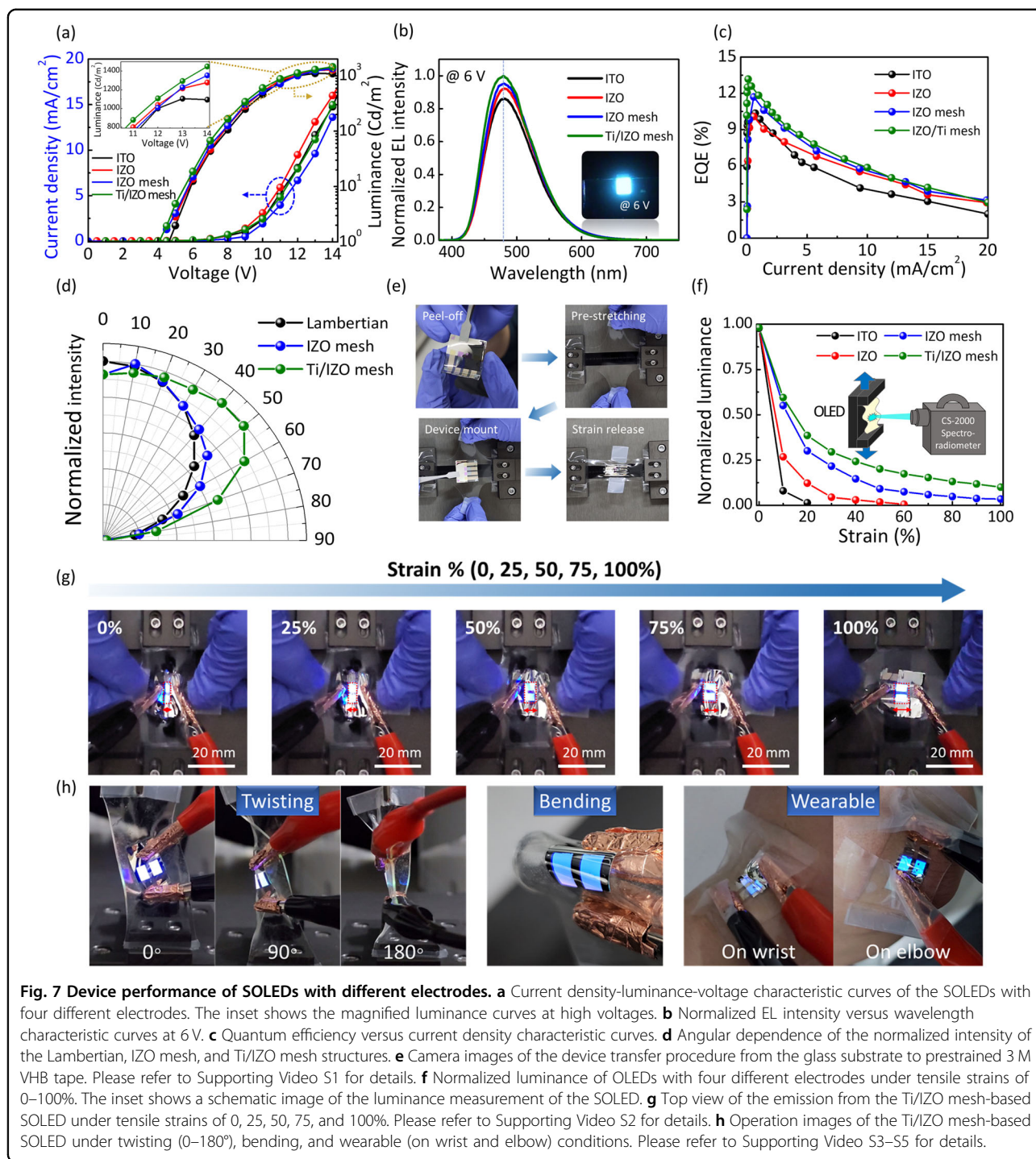
light can be emitted to the outside of the substrate to increase the light extraction intensity, as shown in Fig. 6c. These results reveal that the light enhancement is mainly due to the reduced total internal reflection (TIR) at the interface. In addition, we analyzed the far-field intensity distributions of each OLED device, as shown in Fig. 6d-f. Compared to the IZO-based OLED, the angular-dependent electric field intensity was increased for IZO mesh-based OLEDs due to the wide distribution profiles (or angles) via mesh electrode patterns. To investigate the role of the metal particles, 1000 Ti particles with sizes of 5–50 nm were deposited in a random distribution, and a higher radiation intensity was observed out of the device through the mesh patterns. The light extraction efficiency was found to increase for the entire wavelength as well as for wider angles at 480 nm. These results indicate that the light that is trapped by the waveguide mode can be emitted outside the device by scattering through the Ti particles. Based on these simulation results, we conclude that light outcoupling can be enhanced further via the IZO mesh and Ti particle structure, rather than ITO or IZO planar electrodes, eventually increasing the EQE of the device.

Figure 7a shows the current density–voltage–luminance characteristic curves of the SOLEDs with four different electrodes. Compared to the ITO- and IZO-based OLEDs, the IZO mesh-based OLED exhibited a lower current density at the same applied voltage due to its sharply increased sheet resistance. However, the current density was increased significantly for the Ti/IZO mesh-based



OLED, with a higher slope efficiency than that of the IZO mesh-based OLED, owing to its lowered sheet resistance due to the incorporation of the Ti particles. Regarding luminance, the IZO mesh-based OLEDs with high transmittance and WF-matching with HIL exhibited higher luminance than ITO-based OLEDs. In addition, because of scattering effects and improved conductivity via Ti particles, the maximum luminance of the Ti/IZO mesh-based OLED was observed to be 5.6% and 9.5% higher than those of the IZO mesh and IZO planar electrode-based OLEDs, respectively. Figure 7b shows the normalized electroluminescence (EL) intensity versus wavelength profiles of the OLEDs with four different electrodes measured at 6 V. The peak wavelength was observed to be ~ 480 nm, and its position and the full width at half-maximum did not change significantly for each electrode. The ITO-based OLED exhibited the lowest intensity, and for the rest of the electrodes, the EL intensity was increased in the order of IZO planar-, IZO mesh-, and Ti/IZO mesh-based OLEDs. The inset shows an emission image captured for the Ti/IZO-based OLED. Figure 7c presents the EQE curves as a function of the

current density for the OLEDs with four different electrodes. The maximum EQE values of the devices with the ITO, IZO planar, IZO mesh, and Ti/IZO mesh electrodes were 10.2%, 10.1%, 11.7%, and 13.2%, respectively. This result reveals that the EQE of the Ti/IZO mesh-based OLED was improved by 30 and 13%, respectively, when compared to those of the IZO planar- and IZO mesh-based OLEDs. In addition, to enhance the data stability and reproducibility, statistical data on the standard deviation and mean value of the EQEs measured for twenty different samples are provided in Fig. S9. The average EQE values of the twenty devices were 9.16, 9.09, 10.44 and 12.26%, respectively, while their standard deviations were 0.67, 0.75, 0.99 and 0.88. Figure 7d shows the normalized intensity profiles of each OLED as a function of the viewing angle from 0° to 90° . The intensity of mesh-electrode-based OLEDs was found to be stronger than that of the Lambertian distribution at viewing angles greater than 40° . In particular, the Ti/IZO mesh-based OLED exhibited a much higher intensity with increasing viewing angle than the IZO mesh-based OLED owing to the enhanced light extraction via the Ti particles



embedded in the IZO mesh patterns in addition to the change in the path of light via the patterned mesh structures. Herein, Ti positively affected the optical properties as well as the electrical properties of the electrodes. The random scattering effect increased owing to the island shape of the Ti and the critical angle of TIR, which resulted due to a lower refractive index ($n = 1.9$)

than that of IZO/MoO₃ ($n = 2-2.1$); accordingly, the extracted light as a function of the viewing angle was found to be apparently higher than that of the IZO-mesh-based OLED. The absorption of light via an extremely thin Ti layer appears to be negligible because it is present in the form of islands rather than films. On the other hand, to investigate the effect of the large deviation in the

EL intensity distribution between the OLED with the Ti/IZO mesh electrode and the Lambertian curve, we measured the current efficiency (CE) of the devices with four different electrodes (Fig. S10) and compared it with the EQE of the same devices in Fig. 7c. Furthermore, we calibrated the EQE of the device with a Ti/IZO mesh electrode by considering angular-dependent EL distributions⁴⁴ (Fig. S11) to compare precisely with the CE of the same device. As a result, the EQE curves calculated using a broad angular EL distribution were found to be somewhat different from the measured CE curves, probably because Ti/IZO mesh-based devices have advantages in outcoupling efficiency and sheet resistance, whereas IZO mesh-based devices have advantages in charge balance due to the slightly higher WF of IZO than Ti/IZO. Figure 7e shows the fabrication process for the stretching test. First, the device fabricated on NOA63 substrate was peeled off from the glass substrate, and subsequently, the device was attached to the prestretched 3 M VHB tape. Specifically, after stretching the 3 M VHB tape from 40 mm to 80 mm, a 25-mm-long NOA-based SOLED was attached in the center of the tape, and then, the tape was released to its initial state. Next, the stretching test was repeatedly conducted in the range of 40–80 mm. The emission areas under tensile strains of 0%, 50 and 100% were approximately 3 mm × 4 mm, 4.5 mm × 4 mm and 6 mm × 4 mm, respectively. Figure 7f shows the normalized luminance of the SOLEDs with four different electrodes under strains of 0–100%. The devices with ITO and IZO planar electrodes did not operate under 20 and 60% strains. However, the light emission was maintained under 100% strain for both the IZO mesh and Ti/IZO mesh electrodes, although their normalized luminance was significantly decreased. This result is the first demonstration of the operation of TADF-based blue SOLEDs under 100% strain. The degradation in luminance is attributed to the properties of the TADF material and Al cathode. The luminance of the TADF-based OLED is known to be easily degraded when several tests are performed, even without applying strain. The device performance can also be degraded by the cracking of the Al cathode under strain. However, the efficiency and stability of the SOLED would be further improved if more stable organic and cathode materials were applied. Fig. 7g, h show the operation images of the Ti/IZO mesh-based SOLED under tensile strain (0–100%), twisting at various angles (0–180°), bending, and wearable (on wrist and elbow) conditions. Additionally, these images are supported by video clips (Supporting Video S2–S5). The demonstrated Ti/IZO mesh-based SOLEDs were well operated under various strain conditions due to the excellent mechanical stability of the Ti/IZO mesh electrode. A random deformation test was conducted on the

device to further verify the stability of the proposed device, as shown in Video S6. As a result, the operation of the device was successfully maintained under random deformations (Supporting Video S6). This result indicates that Ti/IZO mesh electrodes provide a high stretchability under various external stresses.

Conclusions

In this study, a highly efficient and stretchable TADF blue OLED was demonstrated using metal-oxide-based mesh electrodes. The proposed Ti/IZO mesh electrode exhibited high transmittance, low resistance, and high stretchability, along with energy band alignment with a MoO₃ HIL, through the optimization of the thickness of the IZO film and the ratio of the open area of the mesh. In particular, the same electrode showed high resistance to strain; no substantial loss when subjected to a strain of 100% and only a 20% resistance change after 1000 stretching cycles. Accordingly, the Ti/IZO mesh electrode-based SOLED stably operated even under 100% tensile strain, and its EQE was improved by 30%, 29%, and 13% compared with those of the planar IZO, ITO, and IZO mesh electrode devices, respectively. Owing to the corrugated metal islands, the waveguide mode at the interface was reduced, and outcoupling was increased, leading to a better intensity in terms of the viewing angle. We believe that by applying the mesh electrode developed in this study, the functionality and quantum efficiency of various optoelectronic devices, including solar cells and LEDs, can be further increased.

Acknowledgements

This study was supported by the National Research Foundation of Korea, funded by the Korean government (No. 2016R1A3B1908249). This work was also supported by LG Display under the LGD-Korea University Incubation Program.

Author contributions

T.H.P. conceived the idea, performed the experiment, and contributed to the drafting of the paper. W.R. developed the device, performed the device structural characterization, analysis and interpretation of results. H.J.L. and N.K. performed the experiment, conducted the mechanical characterization, and prepared the figure legends. K.R.S. and A.R. contributed to scientific discussions regarding this article. T.G.K. conceived the idea, designed the experiments, and supervised the project. All authors discussed the results and revised the manuscript.

Competing interests

The authors declare no competing interests.

Publisher's note

Springer Nature remains neutral with regard to jurisdictional claims in published maps and institutional affiliations.

Supplementary information The online version contains supplementary material available at <https://doi.org/10.1038/s41427-022-00411-6>.

Received: 1 December 2021 Revised: 20 May 2022 Accepted: 26 May 2022.
Published online: 5 August 2022

References

1. Sekitani, T. et al. Stretchable active-matrix organic light-emitting diode display using printable elastic conductors. *Nat. Mater.* **8**, 494–499 (2009).
2. Wang, J. X. et al. Extremely Stretchable Electroluminescent Devices with Ionic Conductors. *Adv. Mater.* **28**, 4490–4496 (2016).
3. Li, L. et al. Recent Advances in Flexible/Stretchable Supercapacitors for Wearable Electronics. *Small* **14**, 1–23 (2018).
4. Salehi, A., Fu, X., Shin, D. H. & So, F. Recent Advances in OLED Optical Design. *Adv. Funct. Mater.* **29**, 1–21 (2019).
5. Yin, D. et al. Roller-Assisted Adhesion Imprinting for High-Throughput Manufacturing of Wearable and Stretchable Organic Light-Emitting Devices. *Adv. Opt. Mater.* **8**, 1–7 (2020).
6. Yin, D. et al. Mechanically robust stretchable organic optoelectronic devices built using a simple and universal stencil-pattern transferring technology. *Light Sci. Appl.* **7**, 35 (2018).
7. Wu, W. Stretchable electronics: functional materials, fabrication strategies and applications. *Sci. Technol. Adv. Mater.* **20**, 187–224 (2019).
8. Wang, J. & Lee, P. S. Progress and Prospects in Stretchable Electroluminescent Devices. *Nanophotonics* **6**, 435–451 (2017).
9. Sekitani, T., Zschieschang, U., Klauk, H. & Someya, T. Flexible organic transistors and circuits with extreme bending stability. *Nat. Mater.* **9**, 1015–1022 (2010).
10. Li, M., Li, H., Zhong, W., Zhao, Q. & Wang, D. Stretchable conductive polypyrrole/polyurethane (PPy/PU) strain sensor with netlike microcracks for human breath detection. *ACS Appl. Mater. Interfaces* **6**, 1313–1319 (2014).
11. Ko, E. H., Kim, H. J., Lee, S. M., Kim, T. W. & Kim, H. K. Stretchable Ag electrodes with mechanically tunable optical transmittance on wavy-patterned PDMS substrates. *Sci. Rep.* **7**, 1–12 (2017).
12. Choi, D. K. et al. Highly efficient, heat dissipating, stretchable organic light-emitting diodes based on a MoO₃/Au/MoO₃ electrode with encapsulation. *Nat. Commun.* **12**, 1–11 (2021).
13. Zhang, Q. et al. Nearly 100% internal quantum efficiency in undoped electroluminescent devices employing pure organic emitters. *Adv. Mater.* **27**, 2096–2100 (2015).
14. Peng, C. et al. Corrugated Organic Light Emitting Diodes Using Low Tg Electron Transporting Materials. *ACS Appl. Mater. Interfaces* **8**, 16192–16199 (2016).
15. Thakur, D. et al. Solution-processed hybrid hosts: A way to explore high triplet energy with admirable current and power efficiency without outcoupling techniques for phosphorescent OLEDs. *J. Mater. Chem. C* **8**, 228–239 (2019).
16. Xu, Z., Tang, B. Z., Wang, Y. & Ma, D. Recent advances in high performance blue organic light-emitting diodes based on fluorescence emitters. *J. Mater. Chem. C* **8**, 2614–2642 (2020).
17. Yoon, J. A. et al. Highly efficient blue organic light-emitting diodes using quantum well-like multiple emissive layer structure. *Nanoscale Res. Lett.* **9**, 1–7 (2014).
18. Wang, L. et al. Efficiency enhancement of flexible OLEDs by using nano-corrugated substrates and conformal Ag transparent anodes. *AIP Adv.* **8**, 055030 (2018).
19. Kim, H. J. et al. Work function and interface control of amorphous IZO electrodes by MoO₃ layer grading for organic solar cells. *Sol. Energy Mater. Sol. Cells* **141**, 194–202 (2015).
20. Ma, Y. & Zhi, L. Graphene-Based Transparent Conductive Films: Material Systems, Preparation and Applications. *Small Methods* **3**, 1800199 (2019).
21. Li, X., Wang, Y., Yin, C. & Yin, Z. Copper nanowires in recent electronic applications: Progress and perspectives. *J. Mater. Chem. C* **8**, 849–872 (2020).
22. Kim, J., Park, J., Jeong, U. & Park, J. W. Silver nanowire network embedded in polydimethylsiloxane as stretchable, transparent, and conductive substrates. *J. Appl. Polym. Sci.* **133**, 1–7 (2016).
23. Fan, X. et al. PEDOT:PSS for Flexible and Stretchable Electronics: Modifications Strategies, and Applications. *Adv. Sci.* **6**, 1900813 (2019).
24. Yang, J. et al. Stretchable, transparent and imperceptible supercapacitors based on Au/MnO₂ nanomesh electrodes. *Chem. Commun.* **55**, 13737–13740 (2019).
25. Lee, H. B., Jin, W. Y., Ovhal, M. M., Kumar, N. & Kang, J. W. Flexible transparent conducting electrodes based on metal meshes for organic optoelectronic device applications: A review. *J. Mater. Chem. C* **7**, 1087–1110 (2019).
26. Guo, C. F., Sun, T., Liu, Q., Suo, Z. & Ren, Z. Highly stretchable and transparent nanomesh electrodes made by grain boundary lithography. *Nat. Commun.* **5**, 1–8 (2014).
27. Jung, J. et al. Moiré-Free Imperceptible and Flexible Random Metal Grid Electrodes with Large Figure-of-Merit by Photonic Sintering Control of Copper Nanoparticles. *ACS Appl. Mater. Interfaces* **11**, 15773–15780 (2019).
28. Sakamoto, K. et al. Highly flexible transparent electrodes based on mesh-patterned rigid indium tin oxide. *Sci. Rep.* **8**, 3–4 (2018).
29. Lee, S. Y., Cho, E. S. & Kwon, S. J. The optical analyses of the multilayer transparent electrode and the formation of ITO/Mesh-Ag/ITO multilayers for enhancing an optical transmittance. *Appl. Surf. Sci.* **487**, 990–999 (2019).
30. Choi, J. et al. Ag fiber/IZO Composite Electrodes: Improved Chemical and Thermal Stability and Uniform Light Emission in Flexible Organic Light-Emitting Diodes. *Sci. Rep.* **9**, 3–9 (2019).
31. Lee, S. M., Chae, J. S., Kim, D. Y. & Choi, K. C. Plasmonic nanomeshes as large-area, low-resistive transparent electrodes and their application to ITO-free organic light-emitting diodes. *Org. Electron.* **15**, 3354–3361 (2014).
32. Hautcoeur, J. et al. Transparency and electrical properties of meshed metal films. *Thin Solid Films* **519**, 3851–3858 (2011).
33. Lee, J., Lee, D., Lim, D. & Yang, K. Structural, electrical and optical properties of ZnO:Al films deposited on flexible organic substrates for solar cell applications. *Thin Solid Films* **515**, 6094–6098 (2007).
34. Pazos-Perez, N., Garcia De Abajo, F. J., Fery, A. & Alvarez-Puebla, R. A. From nano to micro: Synthesis and optical properties of homogeneous spheroidal gold particles and their superlattices. *Langmuir* **28**, 8909–8914 (2012).
35. Lu, C. H. et al. Characteristics and mechanism of tunable work function gate electrodes using a bilayer metal structure on SiO₂ and HfO₂. *IEEE Electron Device Lett.* **26**, 445–447 (2005).
36. Fu, H., Reich, K. V. & Shklovskii, B. I. Hopping conductivity and insulator-metal transition in films of touching semiconductor nanocrystals. *Phys. Rev. B* **93**, 1–12 (2016).
37. Can, M. & Havare et al. Electrical properties of SAM-modified ITO surface using aromatic small molecules with double bond carboxylic acid groups for OLED applications. *Appl. Surf. Sci.* **314**, 1082–1086 (2014).
38. Earmme, T. & Jenekhe, S. A. High-performance multilayered phosphorescent OLEDs by solution-processed commercial electron-transport materials. *J. Mater. Chem.* **22**, 4660–4668 (2012).
39. Qiu, T. et al. Trilayer Nanomesh Films with Tunable Wettability as Highly Transparent, Flexible, and Recyclable Electrodes. *Adv. Funct. Mater.* **30**, 2002556 (2020).
40. Ding, S. et al. One-Step Fabrication of Stretchable Copper Nanowire Conductors by a Fast Photonic Sintering Technique and Its Application in Wearable Devices. *ACS Appl. Mater. Interfaces* **8**, 6190–6199 (2016).
41. Du, X. et al. Transparent and Stretchable Graphene Electrode by Intercalation Doping for Epidermal Electrophysiology. *ACS Appl. Mater. Interfaces* **12**, 56361–56371 (2020).
42. Hu, H. et al. Aligned Silver Nanowires Enabled Highly Stretchable and Transparent Electrodes with Unusual Conductive Property. *Adv. Funct. Mater.* **29**, 1902922 (2019).
43. Yin, Y., Lan, C., Guo, H. & Li, C. Reactive Sputter Deposition of WO₃/Ag/WO₃ Film for Indium Tin Oxide (ITO)-Free Electrochromic Devices. *ACS Appl. Mater. Interfaces* **8**, 3861–3867 (2016).
44. Lee, W. H. et al. Comparison of organic light emitting diode performance using the spectroradiometer and the integrating sphere measurements. *AIP Adv.* **10**, 095011 (2020).